A Biomorphic Whisker Sensor for Aerial Tactile Applications

Chaoxiang Ye, Guido de Croon, Salua Hamaza

***Abstract*— Unmanned air vehicles (UAVs) have traditionally been considered as "eyes in the sky", that can move in three dimensions and need to avoid any contact with their environment. On the contrary, contact should not be considered as a problem, but as an opportunity to expand the range of UAVs applications. In this paper, we designed, fabricated, and characterized a whisker sensor unit based on MEMS barometers suitable for tactile localization on UAVs, featuring lightweight, low stiffness, high sensitivity, a broad sensing range, and scalability. Then, for the challenging task of contact point localization, we propose a Recurrent Multi-output Network (RMN) for predicting 3D contact points under continuous contact conditions to address the problems of non-linearity, hysteresis, and non-injective mapping between signals and contact points by considering time series. In addition, we propose an azimuth prediction loss function which reduces the RMSE by 3.24° compared to L_1 loss. Finally, we conduct experiments on a linear stage to validate the 3D contact point localization capability of the proposed whisker system and model. The results show that our localization can achieve excellent performance, with an inference time of 1.4 ms and a mean error of only 9.18 mm in Euclidean distance within 3D space, laying a robust foundation for future implementation of tactile localization on UAVs. The design files, dataset, and source code are available on: `https://github.com/BioMorphic-Intelligence-Lab/Whisker-3D-Localization`.**

I. INTRODUCTION

Whiskers, also known as vibrissae, are specialized sensory organs of animals like rodents, cats, and seals [1]. They are embedded in follicles and have a rich nerve supply, making them highly sensitive to even slight changes in the surrounding environment. Drawing inspiration from nature, artificial whiskers have been developed as lightweight, sensitive tactile sensors for robots. They empower robots to interact with objects non-intrusively [2], [3]; sense the airflow of surroundings [4]–[6]; and self-vibration [7] through sensitive tactile perception. Advanced technologies have propelled artificial whiskers to perform complex tasks such as object exploration [2], [8] and recognition [2], [9], [10], contact point localization [3], [11], [12], airflow odometry [13], etc.

Whereas most work in the literature has focused on ground robots, tactile interaction can also be beneficial to flying robots. It can enhance UAVs' sensory capabilities on obstacle avoidance, localization, navigation, and even mapping through physical interaction with the environment. These advanced functionalities can empower UAVs to autonomously navigate through challenging environments via non-intrusive tactile feedback. Whiskers for aerial-tactile applications require a different set of attributes than ground robots: 1) a lightweight and compact design that has minimal impact on UAV battery life; 2) low stiffness to enable gentle and non-intrusive interaction with the environment thereby minimizing contact-induced forces; 3) a broad sensing coverage to prevent airborne collisions; 4) high sensitivity to contact in both non-intrusive and long-range situations; 5) high resolution and rapid response time for real-time functioning; and 6) robust contact point localization performance enables accurate navigation decisions to be inferred.

Fig. 1. A size comparison of a tiny UAV ($92 \times 92 \times 29$ mm, 27 g) with a 15 g maximum payload and the proposed whisker sensors ($20 \times 18 \times 200$ mm, 1.52 g).

To the best of our knowledge, only two studies have discussed whisker sensors for potential use in aerial applications [4], [14]. However, these studies primarily focus on airflow sensing rather than tactile sensing, and do not specifically delve into the topic of contact point localization. Research on contact point localization has primarily found implementation on ground robots. For example, [12] employed 3D magnetic sensors to gauge whisker deflections, while [3] extended this approach by introducing the movement of the whisker base over time to accurately determine the precise 2D spatial location of the contact point based on the Kalman Filter. Without relying on the time variation of the moments, [11] and [15] designed tapered whiskers that establish a unique correspondence between three forces and three moments at the base of the whisker and other contact points distributed along the length.

Our primary aim is to develop lightweight, compact, and autonomously operating whiskers that can be easily stacked into an array, and seamlessly integrated with UAVs of varying configurations without compromising UAVs' performance, see Fig. 1. Incorporating low stiffness and an

The authors are with the Biomorphic Intelligence Laboratory & MAVlab, Dept. of Control & Operations, Faculty of Aerospace Engineering, TU Delft, The Netherlands. C.Ye@tudelft.nl

extended sensing area is key to enabling delicate aerial physical interaction with its surroundings, reducing the likelihood of collisions. Commonly used whisker sensing mechanisms, such as those utilizing magnetic [3], [4], [12] and optical sensors [7], [15], [16], often need a substantial base area for mounting and have limited sensitivity. Consequently, these methods do not align well with our objectives. Utilizing MEMS pressure sensors, known for their compact size, lightweight, and high sensitivity, presents a promising approach for our research. Previous studies [14] and [2] successfully applied MEMS-based whisker sensors for tasks such as airflow sensing and binary touch detection. Building on previous research, we designed a MEMS-based whisker sensor for tactile-based aerial applications on UAVs. Our innovation of design features an optimized manufacturing process, reduced weight, compact structure, enhanced sensitivity, and the ability to scale seamlessly for extensive array configurations. Moreover, it provides a larger sensing coverage compared to prior approaches.

Research in whisker perception presents various challenges. Firstly, the utilization of soft material-based MEMS whiskers inherently introduces limitations on precise perception tasks, notably non-linearity and hysteresis in their response [17], Fig. 4. Secondly, the nature of straight and cylindrical whiskers brings about another issue – numerous contact positions yield identical whisker deflections [18], also illustrated in Fig. 4. Consequently, identical moments generate identical signal outputs, exacerbating the complexity of establishing distinct contact point positions based on traditional physical models. To address these challenges, we incorporate Recurrent Neural Networks (RNNs) into contact point localization on whiskers, learning useful features from streaming data. Additionally, we apply a task-specific loss function to account for angle periodicity in azimuth prediction. Ultimately, the 3D contact point output can be efficiently trained using the Recurrent Multi-output Network (RMN), which has fewer parameters, resulting in savings in both training time and computing resources.

The contributions of this study are outlined below:

- We design, fabricate, and characterize a new MEMS-based whisker sensor for contact point localization suitable for aerial robots.
- We propose an RMN for precise 3D contact point localization, addressing hysteresis and non-linearity in response, non-injective mapping between signals and contact points, and resource efficiency.
- We test the sensing sensitivity of our whisker sensor and evaluate the 3D contact point localization performance using a linear stage. The results demonstrate high-precision localization performance with a mean error of only 9.18 mm in Euclidean distance with an inference time of 1.4 ms.

II. Whisker Design and Fabrication

A. Concept

In biological systems, whiskers lack sensors along their length and rely on mechanoreceptors at their base, or follicle, for detection [19], [20]. Upon contact, forces and moments are transmitted, leading to follicle deformation that mechanoreceptors convert into neural signals. Under quasi-static and frictionless conditions, the whisker base experiences three forces and three moments, effectively encompassing all mechanical information that enters the follicle. The importance of measuring moments for contact point detection is highlighted [3], [11], [12], [21], driving the design of a lightweight, compact, highly sensitive, and scalable sensor capable of accurately capturing these mechanical signals based on MEMS barometers in our work.

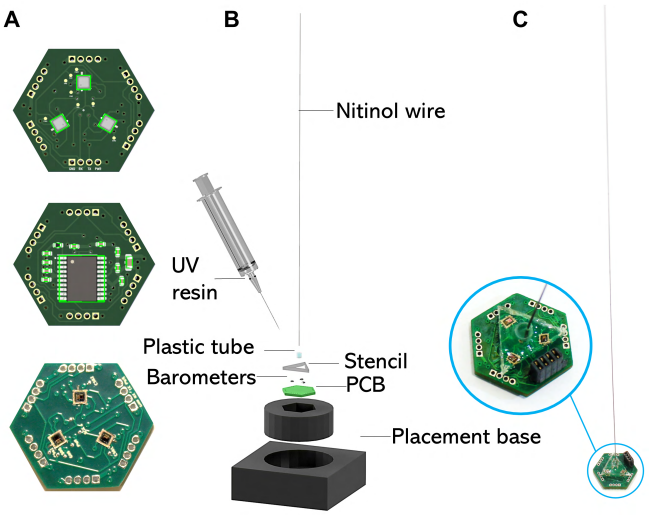

Fig. 2. Whisker design and fabrication. A) Front and Back View of 4-Layer PCB and barometer without package. B) Components of whisker fabrication. The stencil is removed after molding the follicle structure. The placement base serves solely for subsequent characterization and localization experiments. C) Example picture of a whisker sensor.

B. Design

As shown in Figure 2, our system consists of three parts: 1) a nitinol wire serving as a delicate whisker shaft for subtle touch interactions; 2) a follicle structure containing a plastic tube, UV resin, and three MEMS barometers; and 3) an integrated microcontroller PCB for autonomous signal acquisition, processing, and communication. The PCB is composed of four layers (Fig. 2A), with a total thickness of 1.6 mm. Each PCB is purposely shaped like a hexagonal honeycomb, featuring communication ports along each of its sides, which enable flexible and seamless array expansion. For the whisker shaft, we chose a 200 mm length nitinol wire with a 0.4 mm diameter from options including 0.2, 0.4, 0.6, and 0.8 mm diameters by a pre-experiment. This choice guarantees an ample sensing coverage and high sensitivity while keeping the stiffness low. We skip the initial gel cast used in [14]. Instead, we combine the barometer, plastic tube, and whisker root into one unit called the follicle structure sensing unit, making the fabrication process simpler and increasing sensitivity. Contact with the whiskers induces deformation of the follicle, exerting pressure on the mechanoreceptors. The resultant forces and moments can be measured using a MEMS barometer. The weight of the whisker unit is 1.52 g.

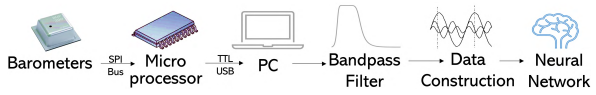

Fig. 3. The sensing pipeline in the whisker sensor system. The output of neural network is 3D contact point prediction.

C. Fabrication

The fabrication process is illustrated in Fig. 2B. We use a reflow oven to solder barometers in 10-pin LGA packages. The metal package covering the MEMS device is then carefully removed to expose the sensing element for microforce detection, unlike [2]. Then, we fix the nitinol wire in a straight manner and maneuver a hot air gun at a velocity of around 5 mm/s at 520 C° for precise programming. A stencil, 2 mm thick, is placed on the PCB to mold the enclosure for the three barometers. A plastic tube, 5 mm in height with outer and inner diameters of 3 and 2 mm respectively, is positioned at the center of the three barometers. The programmed nitinol wire is then carefully lowered into the central axis of the plastic tube, ensuring it aligns perpendicular to the PCB surface. Subsequently, a syringe with a 1.2 mm needle is used to inject 1.5 ml of UV resin along the plastic tube. The resin flows until a uniform surface is formed within the mold, then cured under a UV resin lamp. After that, we applied resin dots around the tube to form a cone shape, ensuring a sturdier mounting for the whisker and enhancing its sensitivity. Any excess resin could cause the barometer to exceed its operational range due to the high sensitivity of barometers.

D. System Integration and Signal Processing

The process of system integration is illustrated in Fig. 3. The chosen sensing unit for our whisker sensor is the BMP390 (BOSCH). To achieve the control, data reading, and initial data processing from the three barometers, we choose an STM32F070F6 (32Kbytes flash memory, 48 MHz CPU) microcontroller. The SPI bus facilitates serial communication between the microcontroller and the barometers. This involves reading sensor data sequentially by lowering the levels of chip select pins in order. For the connection between the microcontroller and the PC, we used the CH340-g (WCH), a USB-TTL serial port converter. In this work, each set included three pressure data points sampled at a rate of 115 Hz. To reduce the drift problem of ambient temperature variations and partial strain recovery in the UV resin, we access the register of BMP390 to apply the temperature compensation coefficients to raw data. Additionally, a first-order Butterworth band-pass IIR filter (0.03 to 5.75 Hz) was applied, effectively eliminating low-frequency drift and high-frequency noise (whisker ringing).

III. Contact Point Localization

A. Problem Definition

Whisker sensors, being soft sensors, are crafted from deformable materials to ensure gentle interaction with objects, minimizing stiffness. However, this softness introduces challenges such as non-linearity and hysteresis in response [17].

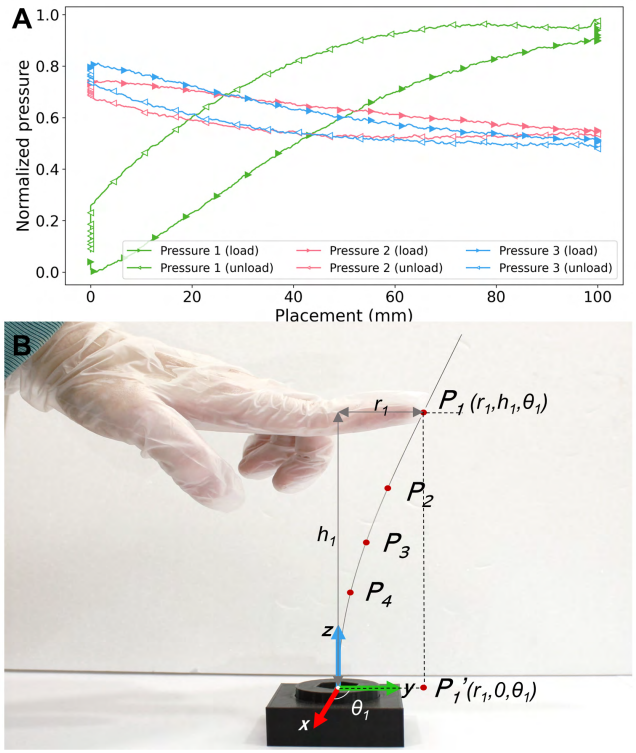

Fig. 4. Challenges in utilizing whisker sensor for contact point localization. (A) Nonlinear and hysteresis response in three-channel signals of the whisker sensor. (B) The whisker causing deflection at contact point P_1 will also register similar signal outputs at subsequent contact points, like P_2, P_3, and P_4. These points are defined in cylindrical coordinates.

Fig. 4A shows the 3 barometers signals' existing hysteresis and nonlinear characteristics of the proposed whisker sensor.

The second problem is depicted in Fig 4B. As discussed in [11], the acquisition of three pressure signals from the follicle structure allows a close correlation to be established with two bending moments, M_x and M_y. While this can calculate whisker deflection [12], it leads to a non-injective mapping due to multiple contact locations P_1, P_2, P_3, and P_4 producing the same deflection and sensor signals. Prior studies have resorted to inferring contact points by assuming the initial contact point and fusing the motion of the whisker base over time [3], [21].

To address these challenges, we propose using the RMN to extract features from time series data, which can accurately predict 3D contact points without requiring additional information. Moreover, we also introduce a loss function that takes into account the periodic nature of the azimuth angle (θ) for 3D contact point localization.

B. Architecture

The proposed model can simultaneously learn to estimate 3D contact points while addressing the issues of nonlinear and hysteresis response and non-injective mapping. As illustrated in Fig. 4B, the 3D contact points are represented in a cylindrical coordinate system. Each point i, denoted as $P_i = \{r_i, h_i, \theta_i\}$, serves as the label for this network.

The RMN's overall architecture is shown in Fig. 5. At time

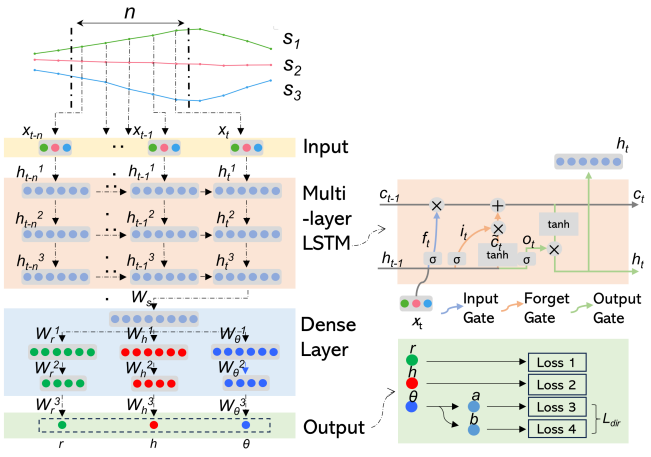

Fig. 5. The architecture of the RMN.

point t, the collected data input to the model is represented as $X_t = \{x_{t-n}, \ldots, x_t\}$, where n is the length of the time window for backtracking. The vector $x_i = \{s_1, s_2, s_3\}$ represents the input data at each time point i, containing three preprocessed barometer signal values. The structure used to capture temporal representation in this model comprises a three-layer Long short-term memory (LSTM) [22]. The detail of the LSTM cell is shown in Fig. 5. The output h_t of the LSTM structure is computed:

$$\begin{aligned} f_t &= \sigma\left(W_f \cdot [h_{t-1}, x_t] + b_f\right) \\ i_t &= \sigma\left(W_i \cdot [h_{t-1}, x_t] + b_i\right) \\ o_t &= \sigma\left(W_o \cdot [h_{t-1}, x_t] + b_o\right) \\ \tilde{C}_t &= \tanh\left(W_g \cdot [h_{t-1}, x_t] + b_g\right) \\ h_t &= o_t \odot \tanh\left(C_t\right) \end{aligned} \tag{1}$$

where i_t, f_t, and o_t denote input gates, forget gates, and output gates, respectively, and W_i, W_f, and W_o are parameter matrices for each of the gates. The state of $\tilde{C}_t$ updates based on the f_t and i_t:

$$C_t = f_t \odot C_{t-1} + i_t \odot \tilde{C}_t \tag{2}$$

where C_{t-1} and C_t are the cell states of the inputs and outputs respectively, and $\odot$ is element-wise multiplication. Next, we feed h_t into a Dense structure comprising four fully connected layers to predict 3D localization points. The parameters of the initial fully connected layer W_s are shared, while the subsequent layers have independent parameters W_r^i,W_h^i,W_θ^i where $i \in \{1, 2, 3\}$. This configuration allows our network to more effectively fit the data. The total loss function is presented:

$$L_{\text{total}} = \frac{1}{N}\sum_{i}^{N}\left\|r^i - r_{gt}^i\right\|_\gamma + \frac{1}{N}\sum_{i}^{N}\left\|h^i - h_{gt}^i\right\|_\gamma + L_{\text{dir}} \tag{3}$$

where $\{r^i, r_{gt}^i\}$ and $\{h^i, h_{gt}^i\}$ represent the estimated and ground truth values for radial distance (r) and height (h), N is the total number of data samples, and L_{dir} is the loss function for the directional regression task. The $\| \ \|_\gamma$ is the distance between the prediction and the ground truth value, with the norm given by γ.

C. Loss Function

For the prediction of r and h, we can build a regression task by forming a smooth, continuous and injective regression loss in Euclidean space, $\left\|r^i - r_{gt}^i\right\|_\gamma$ and $\left\|h^i - h_{gt}^i\right\|_\gamma$. After comparing with L_2, we found that the L_1 loss function is more robust on our task, so we set γ to 1.

However, predicting θ poses a more significant challenge. First, directly regressing angles using $L_1 = \| \ \|_1$ or $L_2 = \| \ \|_2$ loss functions is a simple and effective approach [23]. The advantage of this method lies in its smooth and continuous loss functions, which are easy to optimize. However, it cannot accurately represent angular losses due to their periodic nature, which 2π and 0 are the same but would give large errors. Taking inspiration from quaternions, which offer a smooth and continuous way to represent rotations [24], [25], we project ground truth angles onto a unit circle constraint in two dimensions, denoted as $a_{gt}^i = \cos\left(\theta_{gt}^i \cdot \frac{\pi}{180}\right)$ and $b_{gt}^i = \sin\left(\theta_{gt}^i \cdot \frac{\pi}{180}\right)$. This technique incorporates angle information within a two-dimensional space, effectively addressing the periodicity issue and potential optimization convergence to extreme labels. However, this method lacks injectiveness, as different $\|(a^i, b^i)\|_2$ values under the same angle can result in varying errors. Otherwise, we constrain it within a specific range [0,r_c], where r_c is the regularization parameter set to 0.8 in this paper. This regularization approach partially restricts the parameter space, slightly addressing the non-injectiveness issue and improving gradients when the output approaches the target. The loss function is as follows:

$$L_{dir} = \frac{1}{N}\sum_{i=1}^{N}\left(\left\|a^i - a_{gt}^i\right\|_2 + \left\|b^i - b_{gt}^i\right\|_2\right) \tag{4}$$

where we constrain the $\|(a^i, b^i)\|_2 \leq r_c$.

D. Simultaneous Learning

In our model, we simultaneously learn three labels: r, h, and θ. The model shares parameters except for the last three fully connected layers. This approach conserves computational resources to enable high-resolution real-time localization. We enhance the performance of the model by normalizing the prediction targets r and h to the range [0,1]. This normalization helps mitigate the issue of imbalanced weights. The overall loss function can be expressed as:

$$\begin{aligned} L_{\text{total}} = \frac{1}{N}\Bigg(\sum_{i=1}^{N}\left\|\frac{r^i - r_{gt}^i}{\sigma_r}\right\| + \left\|\frac{h^i - h_{gt}^i}{\sigma_h}\right\| + \ \cdots \\ + \left\|a^i - a_{gt}^i\right\|_2 + \left\|b^i - b_{gt}^i\right\|_2\Bigg) \end{aligned} \tag{5}$$

where $\|(a^i, b^i)\|_2 \leq r_c$ and σ_r and σ_h are normalization factors to standardize r_{gt}^i and h_{gt}^i to the range [0,1].

IV. Experiments

A. Experimental Setup

We tested the whisker system performance using a setup that measured both force and position at various contact

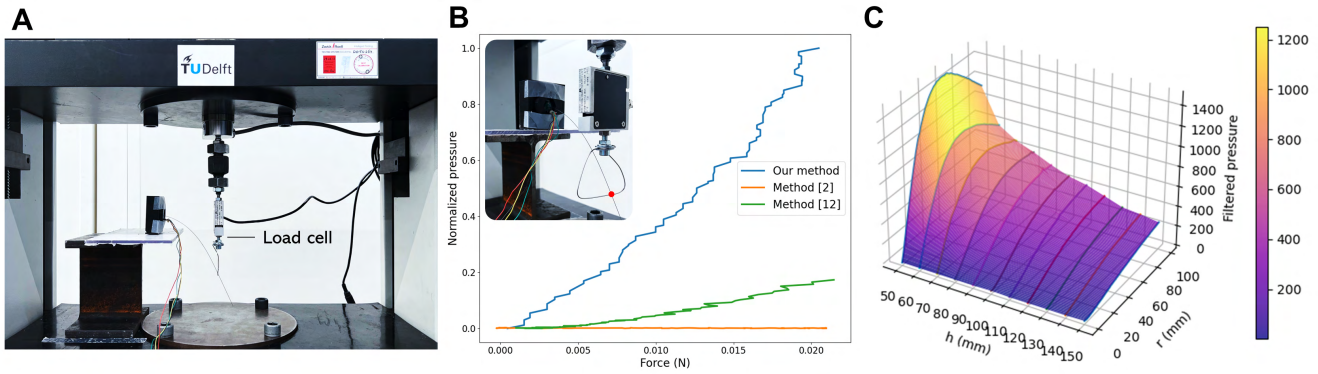

Fig. 6. A) Experimental setup for contact force sensing and contact point localization. B) Comparing contact force to normalized pressure data in three different design concepts. C) Isometric surface plots illustrating filtered pressure data as a function of r (0 to 100 mm) at various h.

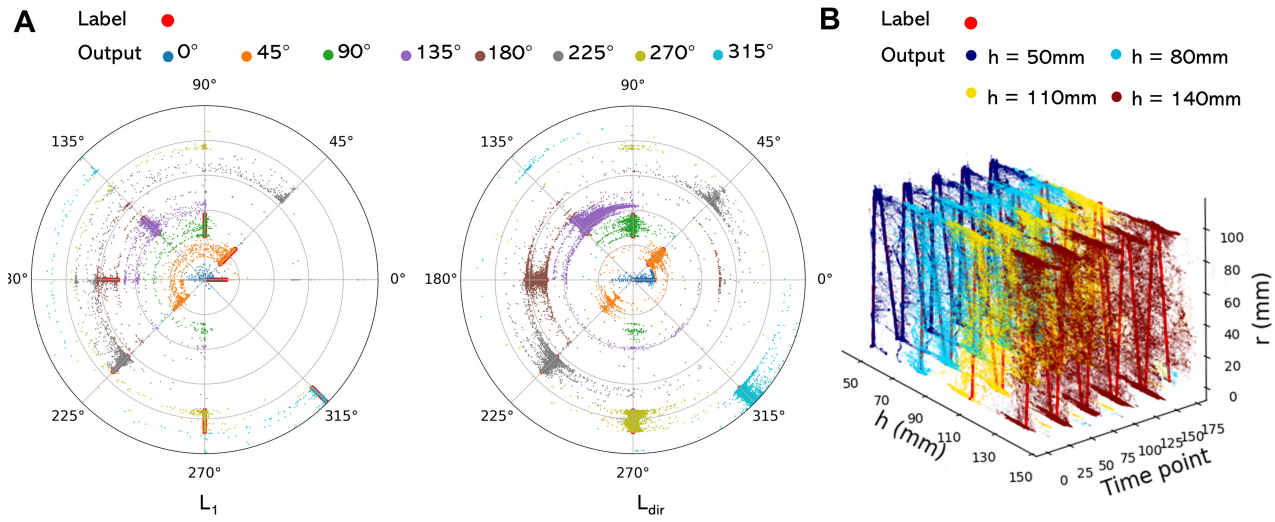

Fig. 7. (A) Comparison of single outputs θ trained with L_1 and L_{dir} against labels. The MAE and RMSE of L_1 are 3.40 and 23.77 mm, and the MAE and RMSE of L_{dir} are 3.21 and 20.53 mm. L_{dir} shows better robustness after considering periodicity. (B) The outputs and corresponding labels for r overtime at h of 5, 8, 11, and 14 mm for all θ, which selects parts of all h to show the results more clearly.

points (Fig. 6A). A linear stage and 10N load cell (both from Zwick Roell) with a slender rod were employed to ensure the force acted purely vertically on the whisker shaft. The setup included a 3D custom-printed placement base that allowed adjustments to different θ, see Fig. 2B. The base was attached to a plastic plate with a ruler for precise height adjustments with respect to the whisker's base.

In the first experiment, we compare the sensitivity of our whisker sensor with that of two replica whiskers from the literature. The two replica whiskers examined here have the same design concept as those described in [2], [14]. The 3 whiskers were placed in identical orientations on the base, and a force characterization test was conducted. Force was applied by raising the linear stage at $h = 50$ mm, $\theta = 180°$, and force signals were reading from the load cell.

In the second experiment, continuous r were applied to the whisker shaft, ranging from 0 to 100 mm at a speed of 10 mm/s. Each trial encompassed loading and unloading phases, with a 5-second hold at $r \in \{0, 100\}$ mm respectively. We repeated these steps at 10 mm intervals, covering the range of $h \in [50, 150]$ mm. We also conducted similar procedures at different θ by rotating the internal components of the placement base in 45-degree increments. The complete dataset consists of 88 combinations (11 heights h, 8 angles θ), each repeated 30 times. Consequently, the evaluated sensing area encompasses a cylindrical sensing range defined as $\{(r, \theta, z) \,|\, 0 \leq r \leq 100\,mm,\, 0 \leq \theta \leq 360°,\, 50 \leq z \leq 150\,mm\}$, providing a solid basis for contact point localization on UAVs.

B. Contact Force Sensing

We conducted experiments to measure contact force using three distinct sensor designs, Fig. 6B. Both methods [12] and our proposed approach exhibit a nearly linear relationship between sensor data and applied force at the loading pressure phase. However, method [2] struggles to detect forces below 0.02 N, particularly given the stiffness of our nitinol wire. As a result, within our own controlled manufacturing environment, our design demonstrates superior sensitivity. Additionally, we analyze the signal output of our whisker under an angle θ of 180° at various h while exerting increasing pressure with r (Fig. 6C). Notably, the filtered pressure vs. r curve exhibits a steeper incline as the contact

TABLE I

3D POINT LOCALIZATION RESULTS WITH A MEAN EUCLIDEAN DISTANCE ERROR OF 9.18 MM AND INFERENCE TIME OF 1.4 MS

Test Error	Radial Distance r (mm)	Height h (mm)	Azimuth angle $\theta(\circ)$
MAE	5.00	5.37	4.06
RMSE	10.74	9.03	20.8

TABLE II

COMPARISON OF r PREDICTION RESULTS FOR DIFFERENT TIME SERIES WITH $\theta = 0°$ AND $h = 15$ MM

Time Series	1	10	20	30	40	50
RMSE (mm)	14.13	11.84	10.39	9.19	8.02	8.18

point approaches the whisker base. This observation suggests that by taking the time series into account, we may be able to deduce the precise 2D position of the contact point. However, it is worth noting that in cases where the contact point is extremely close to the base, the r becomes too large, leading to a lower pressure reading. This occurs when the whisker loses contact with the perpendicular surface, resulting in a shift from applying a direct force to a lateral force.

C. Implementation and Training

We structured the data into $[40, 3]$ arrays with a sliding window step of 1, where 40 represents the number of time series data and 3 denotes 3 signal channels. Labels were determined based on the value at the last time point, maintaining a signal frequency of 115 Hz. The dataset was then split into training, validation, and test sets. The training set contains 6,068,046 frames, while both the validation and test sets have 1,504,834 frames each. The validation set is solely employed for hyperparameter selection, which can be found on our GitHub repository. Notably, the training set was randomly shuffled in each epoch. All models were trained on an NVIDIA RTX 3050 GPU using the Adam optimizer with a learning rate of 1×10^{-4}. In the experiments for evaluating the different angle loss functions, only the labels of θ were used. For 3D contact point localization task, all labels were trained simultaneously. All training spanned 30 epochs, with the best-performing model across all epochs being saved.

D. Results on Contact Point Localization

We begin by assessing the effectiveness of the proposed loss functions L_{dir}. The results generated by L_{dir}, with Mean Absolute Error (MAE) and Root Mean Square Error (RMSE) values of 3.21 and 20.53 mm respectively, exhibit a smoother and more reliable progression when compared to those produced by L_1, which have MAE and RMSE values of 3.40 and 23.77 mm. L_1 tends to excessively bias the angle optimization in one particular direction, leading to a noticeable absence of output labels within the range of 0°-315°, see Fig. 7A. In this context, L_{dir} yields a softer output, directly contributing to a reduction in RMSE.

Next, we evaluated the RMN performance for the simultaneous estimation of 3D contact points. We illustrate the predicted and ground truth of r overtime at 5, 8, 11, 14 mm h of all of the θ out of all results, Fig 7B. This evaluation showcases that our architecture can address whisker's non-linearity and hysteresis challenges. Moreover, this figure provides clear evidence of the performance we achieve in distinguishing different contact point outputs under the same whisker deflection. Each contact point can be predicted precisely. This reaffirms the effectiveness of our approach based on the RNN, which exclusively relies on the input from the sensor signals. Table I presents the 3D contact point localization results, which exhibit impressive performance, with MAE of 5.00 mm, 5.37 mm, and 4.06 ° for r, h, and θ respectively. Additionally, the RMSEs are measured at 10.79 mm, 9.03 mm, and 20.8 ° for the respective dimensions. The mean error of the Euclidean distance in three-dimensional space was calculated to be only 9.18 mm. Our model achieves an inference time of 1.4 ms, perfectly aligning with the 115 Hz signal sampling frequency requirement.

In addition, we further investigated the impact of time series data on model performance. This result pertains to the prediction of r using exclusively the data with an θ of 0° and a h of 15 mm over various r, see Table II. When RNN is not utilized (time series set to 1), the model encounters difficulties in handling the non-linearity and hysteresis challenges posed by the whisker sensor. Setting the time series to 40 represents our initial choice, striking a balance between computational resources and model performance.

V. CONCLUSIONS

In this work, we tried to address the significant challenge of integrating a whisker sensor onto a micro air vehicle (UAV) for enhanced environmental interaction. We have successfully designed, fabricated, and characterized a MEMS-based whisker sensor unit tailored to UAV requirements. This sensor unit stands out for its lightweight, low stiffness, high sensitivity, broad sensing range, scalability, and rapid response. To achieve precise tactile localization on a UAV, we introduced an RMN to tackle the inherent non-linearity, hysteresis, and non-injective mapping challenges posed by soft whiskers. Furthermore, we incorporated an azimuth prediction loss function to effectively consider the periodic nature of angles, enhancing the robustness of the model. Our experiments, conducted on a linear platform, demonstrate exceptional performance in 3D contact point localization within a broad perceptual coverage of $\{(r, \theta, z) \,|\, 0 \leq r \leq 100\,mm,\ 0 \leq \theta \leq 360°,\ 50 \leq z \leq 150\,mm\}$. The results demonstrate high precision localization performance with a mean error of only 9.18 mm in Euclidean distance with an inference time of 1.4 ms

To conclude, our study lays a robust foundation for advancing aerial tactile localization, opening up exciting possibilities for enhanced interaction with complex environments.

ACKNOWLEDGMENT

The authors would like to thank Suryansh Sharma and Erik van der Horst for assisting with the PCB debugging phase.

REFERENCES

[1] A. S. Ahl, "The role of vibrissae in behavior: a status review," *Veterinary research communications*, vol. 10, no. 1, pp. 245–268, 1986.

[2] C. Xiao, S. Xu, W. Wu, and J. Wachs, "Active multiobject exploration and recognition via tactile whiskers," *IEEE Transactions on Robotics*, vol. 38, no. 6, pp. 3479–3497, 2022.

[3] M. A. Lin, E. Reyes, J. Bohg, and M. R. Cutkosky, "Whisker-inspired tactile sensing for contact localization on robot manipulators," in *2022 IEEE/RSJ International Conference on Intelligent Robots and Systems (IROS)*. IEEE, 2022, pp. 7817–7824.

[4] S. Kim, R. Kubicek, A. Paris, A. Tagliabue, J. P. How, and S. Bergbreiter, "A whisker-inspired fin sensor for multi-directional airflow sensing," in *2020 IEEE/RSJ International Conference on Intelligent Robots and Systems (IROS)*. IEEE, 2020, pp. 1330–1337.

[5] A. Tagliabue, A. Paris, S. Kim, R. Kubicek, S. Bergbreiter, and J. P. How, "Touch the wind: Simultaneous airflow, drag and interaction sensing on a multirotor," in *2020 IEEE/RSJ international conference on intelligent robots and systems (IROS)*. IEEE, 2020, pp. 1645–1652.

[6] T. Kim, H.-S. Shin, K.-H. Nam, S. Bergbreiter, and Y.-L. Park, "Soft airflow sensors with artificial hair structures and printed ionogel channels for wind gust detection for small uncrewed vehicles," *IEEE/ASME Transactions on Mechatronics*, 2023.

[7] T. A. Kent, S. Kim, G. Kornilowicz, W. Yuan, M. J. Hartmann, and S. Bergbreiter, "Whisksight: A reconfigurable, vision-based, optical whisker sensing array for simultaneous contact, airflow, and inertia stimulus detection," *IEEE Robotics and Automation Letters*, vol. 6, no. 2, pp. 3357–3364, 2021.

[8] M. J. Pearson and M. Salman, "Active whisker placement and exploration for rapid object recognition," in *2019 IEEE/RSJ International Conference on Intelligent Robots and Systems (IROS)*. IEEE, 2019, pp. 672–677.

[9] C. W. Fox, B. Mitchinson, M. J. Pearson, A. G. Pipe, and T. J. Prescott, "Contact type dependency of texture classification in a whiskered mobile robot," *Autonomous Robots*, vol. 26, pp. 223–239, 2009.

[10] N. F. Lepora, M. Evans, C. W. Fox, M. E. Diamond, K. Gurney, and T. J. Prescott, "Naive bayes texture classification applied to whisker data from a moving robot," in *The 2010 International Joint Conference on Neural Networks (IJCNN)*. IEEE, 2010, pp. 1–8.

[11] H. Emnett, M. Graff, and M. Hartmann, "A novel whisker sensor used for 3d contact point determination and contour extraction," in *Robotics Science and Systems*, vol. 14, no. June 2018, 2018.

[12] S. Kim, C. Velez, D. K. Patel, and S. Bergbreiter, "A magnetically transduced whisker for angular displacement and moment sensing," in *2019 IEEE/RSJ International Conference on Intelligent Robots and Systems (IROS)*. IEEE, 2019, pp. 665–671.

[13] A. Tagliabue and J. P. How, "Airflow-inertial odometry for resilient state estimation on multirotors," in *2021 IEEE International Conference on Robotics and Automation (ICRA)*. IEEE, 2021, pp. 5736–5743.

[14] W. Deer and P. E. Pounds, "Lightweight whiskers for contact, pre-contact, and fluid velocity sensing," *IEEE Robotics and Automation Letters*, vol. 4, no. 2, pp. 1978–1984, 2019.

[15] T. A. Kent, H. Emnett, M. Babaei, M. J. Hartmann, and S. Bergbreiter, "Identifying contact distance uncertainty in whisker sensing with tapered, flexible whiskers," in *2023 IEEE International Conference on Robotics and Automation (ICRA)*. IEEE, 2023, pp. 607–613.

[16] N. F. Lepora, M. Pearson, and L. Cramphorn, "Tacwhiskers: Biomimetic optical tactile whiskered robots," in *2018 IEEE/RSJ International Conference on Intelligent Robots and Systems (IROS)*. IEEE, 2018, pp. 7628–7634.

[17] S. Han, T. Kim, D. Kim, Y.-L. Park, and S. Jo, "Use of deep learning for characterization of microfluidic soft sensors," *IEEE Robotics and Automation Letters*, vol. 3, no. 2, pp. 873–880, 2018.

[18] L. A. Huet, J. W. Rudnicki, and M. J. Hartmann, "Tactile sensing with whiskers of various shapes: Determining the three-dimensional location of object contact based on mechanical signals at the whisker base," *Soft robotics*, vol. 4, no. 2, pp. 88–102, 2017.

[19] M. Szwed, K. Bagdasarian, B. Blumenfeld, O. Barak, D. Derdikman, and E. Ahissar, "Responses of trigeminal ganglion neurons to the radial distance of contact during active vibrissal touch," *Journal of neurophysiology*, vol. 95, no. 2, pp. 791–802, 2006.

[20] S. Ebara, K. Kumamoto, T. Matsuura, J. E. Mazurkiewicz, and F. L. Rice, "Similarities and differences in the innervation of mystacial vibrissal follicle–sinus complexes in the rat and cat: a confocal microscopic study," *Journal of Comparative Neurology*, vol. 449, no. 2, pp. 103–119, 2002.

[21] J. H. Solomon and M. J. Hartmann, "Extracting object contours with the sweep of a robotic whisker using torque information," *The International Journal of Robotics Research*, vol. 29, no. 9, pp. 1233–1245, 2010.

[22] S. Hochreiter and J. Schmidhuber, "Long short-term memory," *Neural computation*, vol. 9, no. 8, pp. 1735–1780, 1997.

[23] S. Wang, R. Clark, H. Wen, and N. Trigoni, "Deepvo: Towards end-to-end visual odometry with deep recurrent convolutional neural networks," in *2017 IEEE international conference on robotics and automation (ICRA)*. IEEE, 2017, pp. 2043–2050.

[24] A. Kendall and R. Cipolla, "Geometric loss functions for camera pose regression with deep learning," in *Proceedings of the IEEE conference on computer vision and pattern recognition*, 2017, pp. 5974–5983.

[25] A. Kendall, M. Grimes, and R. Cipolla, "Posenet: A convolutional network for real-time 6-dof camera relocalization," in *Proceedings of the IEEE international conference on computer vision*, 2015, pp. 2938–2946.